Tuning parameters of a sea ice model using machine learning

Anton Korosov[1], Yue Ying[1], and Einar Ólason[1]

[1]Nansen Environmental and Remote Sensing Centre, Jahnebakken 3, 5007, Bergen, Norway

Correspondence: Anton Korosov (anton.korosov@nersc.no)

Abstract.

We developed a new method for tuning sea ice rheology parameters, which consists of two components: a new metric for characterising sea ice deformation patterns and an ML-based approach for tuning rheology parameters. We applied the new method to tune the parametrisation of the brittle Bingham-Maxwell rheology (BBM) implemented and used in the next-generation sea-ice model (neXtSIM). As a reference dataset, we used sea ice drift and deformation observations from the Radarsat Geophysical Processing System (RGPS).

The metric characterises a field of sea ice deformation with a vector of values. It includes well-established descriptors such as the mean and standard deviation of deformation, the structure-function of the spatial scaling analysis, and the density and intersection of linear kinematic features (LKFs). We added more descriptors to the metric that characterise the pattern of ice deformation, including image anisotropy and Haralick texture features. The developed metric can describe ice deformation from any model or satellite platform.

In the parameter tuning method, we first run an ensemble of neXtSIM members with perturbed rheology parameters and then train a machine-learning model using the simulated data. We provide the descriptors of ice deformation as input to the ML model and rheology parameters as targets. We apply the trained ML model to the descriptors computed from RGPS observations. The developed ML-based method is generic and can be used to tune the parameters of any model.

We ran experiments with tens of members and found optimal values for four neXtSIM BBM parameters: scaling parameter for ridging ($P_0 \approx 5.1$ kPa), cohesion at the reference scale ($c_{\text{ref}} \approx 1.2$ MPa), internal friction angle tangent ($\mu \approx 0.7$), ice–atmosphere drag coefficient ($C_A \approx 0.00228$). A NeXtSIM run with the optimal parametrisation produces maps of sea ice deformation visually indistinguishable from the RGPS observations. These parameters exhibit weak interannual drift related to changes in sea ice thickness and corresponding changes in ice deformation patterns.

1 Introduction

Sea-ice dynamics in highly compact ice result from the interaction between surface stress on the ice supplied by wind and ocean currents and the emerging internal stress in the ice. In sea-ice models, the internal stress is calculated by a set of equations commonly referred to as rheology. Virtually all large-scale sea-ice models used for sea-ice forecasting and climate modelling use the so-called viscous-plastic (VP) rheology of Hibler (1979), or more numerically efficient derivatives thereof.

The free parameters of the VP rheology have been estimated in various traditional sensitivity experiments (e.g. Panteleev et al., 2020, 2023), and their values are generally considered fixed by the community today.

A new branch of brittle rheologies has been proposed and extended by Girard et al. (2011), Dansereau et al. (2016), and Ólason et al. (2022), with the latest version, the brittle Bingham-Maxwell rheology (BBM) implemented and used in the next

30 generation sea-ice model, neXtSIM (e.g. Rampal et al., 2016, 2019). NeXtSIM, with the BBM rheology, has already been used in several scientific studies (e.g. Boutin et al., 2022, 2023; Korosov et al., 2023; Regan et al., 2023) and is used for operational sea-ice forecasts (Williams et al., 2021), and BBM has been implemented in SI3, the sea-ice component of the NEMO model (Brodeau et al., 2024). However, the free parameters of BBM have only been briefly explored, and their range and relation to other model components and parameters remain unclear.

35 The BBM rheology, like the other brittle rheologies, is a damage-propagation model. It parameterises the density of fractures (the mechanical weakness of sea ice) at the sub-grid scale with a scalar damage variable. In this framework, undamaged ice is fully elastic, and damage increases when the local stresses reach the Mohr-Coulomb failure criterion. An increase in damage results in a decrease in elasticity, simulating the fracturing of the ice. Once fractured, the ice can also deform viscously, simulating the permanent deformation of fractured ice. This permanent viscous deformation is limited in convergence by

40 resistance to ridge formation, which is also accounted for by the BBM rheology.

As pointed out in Ólason et al. (2022), BBM has many parameters, some well-defined constants and some poorly constrained. These parameters strongly and nonlinearly impact the patterns of sea ice drift and deformation simulated by the model. Visually, the differences between observed and simulated deformation fields can guide the selection of a model parameter value. Still, such manual tuning can become complicated when several parameters must be considered. This work aims to develop a set

45 of metrics for quantitative comparison of the simulated and observed sea ice deformation fields and to use these metrics for tuning BBM parameters utilising a deep learning approach.

2 A brief introduction of BBM rheology

The constitutive model of BBM consists of a parallel dashpot and a friction element, connected in series with a spring (see Fig. 2.a in Ólason et al. (2022)). The spring represents elastic ice deformation, the dashpot viscous deformation when the ice

50 is fractured, and the friction element represents the resistance of broken ice to ridge formation. In a simple 1D case, these regimes can be summarised as follows (with σ, σ_E and σ_v denoting total, elastic and viscous internal stresses, and ε, ε_E and ε_v, total, elastic and viscous deformations). Note that due to the serial connectivity, the elastic stress always equals the total stress $\sigma_E = \sigma$.

- Sea ice is undamaged, viscous stress is zero, and total deformation is fully reversible (elastic): $d = 0$, $\sigma_v = 0$, $\varepsilon = \varepsilon_E$.

55 - Ice is damaged and diverging; the friction element is inactive and, therefore, the viscous stress equals the elastic and the total stress. Deformation is both elastic and viscous: $d > 0$, $\sigma > 0$, $\sigma_v = \sigma_E = \sigma$, $\varepsilon = \varepsilon_E + \varepsilon_v$

- Ice is damaged and converging with weak internal stress, the friction element is active, viscous stress is zero, and all deformations are elastic. $d > 0$, $P_{\max} < \sigma < 0$, $\sigma_v = 0$; $\varepsilon = \varepsilon_E$

- Ice is damaged and converging with strong internal stresses, the friction element is inactive and, therefore, the viscous stress is equal to the elastic and the total stress, deformation is both elastic and viscous: $d > 0$, $\sigma < P_{\max}$, $\sigma_v = \sigma - P_{\max}$; $\varepsilon = \varepsilon_E + \varepsilon_v$

Accounting for two components of the internal stress tensor (normal stress, σ_N and tangent stress, τ), we can generalise the equation for the viscous stress as follows:

$$\sigma_v = (1 + \widetilde{P})\sigma, \tag{1a}$$

$$\widetilde{P} = \begin{cases} \frac{P_{\max}}{\sigma_N} & \text{for } \sigma_N < -P_{\max}, \\ -1 & \text{for } -P_{\max} < \sigma_N < 0, \\ 0 & \text{for } \sigma_N > 0. \end{cases} \tag{1b}$$

where the threshold $P_{\max}$ separates the elastic and visco-elastic regimes and can be computed following the results of Hopkins (1998) and Hibler (1979):

$$P_{\max} = P_0 \left(\frac{h}{h_0} \right)^H e^{-C(1-A)}, \tag{2}$$

where $h_0 = 1$ m is a constant reference thickness, $H = 3/2$ is the exponent of the compression factor, P_0 is a constant reference stress, C is compaction parameter, A is ice concentration and h is thickness.

The time derivative of total stress (see details in Olason et al., 2022) is

$$\dot{\sigma} = E\mathbf{K} : \dot{\varepsilon} - \frac{\sigma}{\lambda} \left(1 + \widetilde{P} + \frac{\lambda \dot{d}}{1-d} \right), \tag{3}$$

where elasticity is a function of damage and concentration:

$$E = E_0(1-d)e^{-C(1-A)}, \tag{4}$$

$\mathbf{K} : \dot{\varepsilon}$ is the stiffness tensor operation:

$$\begin{pmatrix} (\mathbf{K} : \dot{\varepsilon})_{11} \\ (\mathbf{K} : \dot{\varepsilon})_{22} \\ (\mathbf{K} : \dot{\varepsilon})_{12} \end{pmatrix} = \frac{1}{1-\nu^2} \begin{pmatrix} 1 & \nu & 0 \\ \nu & 1 & 0 \\ 0 & 0 & 1-\nu \end{pmatrix} \begin{pmatrix} \dot{\varepsilon}_{11} \\ \dot{\varepsilon}_{22} \\ \dot{\varepsilon}_{12} \end{pmatrix}, \tag{5}$$

λ is the viscous relaxation time:

$$\lambda = \lambda_0(1-d)^{\alpha-1}, \tag{6}$$

with E_0 (undamaged elasticity), ν (Poisson's ratio), λ_0 (undamaged viscous relaxation time, and $\alpha > 0$, being free parameters.

Table 1. BBM rheology parameters.

Parameter	symbol	value
Undamaged elasticity	E_0	5.96×10^8 Pa
Undamaged viscous relaxation time	λ_0	1×10^7 s
Reference thickness ???	h_0	1 m
Damage parameter	α	5
Compaction parameter	C	-28
Scaling parameter for ridging	P_0	10 kPa
Cohesion at the reference scale	c_{ref}	1 MPa
Poisson's ratio	ν	1/3
Internal friction angle tangent	μ	0.7
Exponent of compression factor	H	3/2
Ice–atmosphere drag coefficient	C_a	2.0×10^{-3}

80   Damaging occurs in the BBM rheology whenever the simulated stress in a grid cell or element is outside the failure envelope or yield curve. The failure envelope of the BBM rheology is the Mohr-Coulomb criterion:

$$\tau = \mu \sigma_N + c, \tag{7}$$

where μ is the internal friction coefficient and c is the cohesion. Following Bouillon and Rampal (2015), we let the cohesion scale with model resolution as

$$85 \quad c \sim c_{\text{ref}} \sqrt{\frac{l_{\text{ref}}}{\Delta x}}, \tag{8}$$

where Δx is the distance between model node points, and c_{ref} is the cohesion at the reference length scale, $l_{\text{ref}} = 10$ cm, where the cohesion was measured to be of the order of 1 MPa Schulson et al. (2006).

The aforementioned parameters of the neXtSIM BBM rheology are summarised in Table 1. According to Ólason et al. (2022), such parameters as P_0 and c_{ref} require proper tuning using satellite observations at large spatial and temporal scales.

90 **3 Data**

We used the Lagrangian sea ice motion data from the Radarsat Geophysical Processing System (RGPS) (Kwok et al., 2008) for tuning the above rheology parameters. The dataset contains trajectories of virtual buoys tracked using pattern-matching techniques on SAR imagery from Radarsat-2. The buoys are initialised by RGPS in mid-December in the western Arctic on a regular grid with 10 km spacing on individual SAR images. The position of each virtual buoy is tracked from one image to
95 another overlapping image during the entire winter season (December – May). The trajectory is terminated if a virtual buoy cannot be tracked due to a loss of similarity between SAR images or the absence of images. New virtual buoys are initialised in the regions with low density of the tracked buoys that appear due to sea ice divergence or disappearance of older buoys.
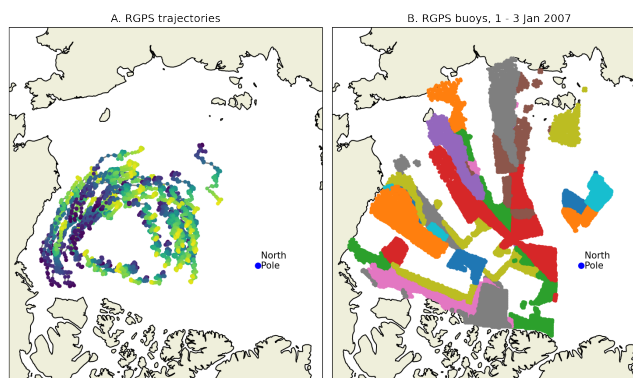
Figure 1. A. Example trajectories of virtual buoys detected on Radarsat-2 data by the RGPS system between 5th December 2006 and 15 May 2007. **B.** Position of all virtual buoys on images SAR images acquired between 1st and 3rd Jan 2007. Points are coloured by the time of image acquisition.

The average time between overlapping Radarsat-2 image acquisitions is three days but may vary from 0.5 to 10 days. Therefore, the timing of virtual buoy positions is highly heterogeneous, even for neighbour trajectories. Figure 1.A shows examples of RGPS trajectories spanning 150 – 180 days, and 1.B shows positions of virtual buoys detected on SAR images acquired between 1st and 3rd Jan 2007. Points are coloured by the time of image acquisition. The plot illustrates how heterogeneous the RGPS Lagrangian ice motion data is in space and time.

4 Methodology

4.1 Overview of the parameter tuning algorithm

In our approach, we compute a set of descriptors that characterise patterns in the fields of observed and simulated sea ice deformation. Since the correlation between the descriptors and model parameters is weak (see Fig. 9), we could not use linear regression-based methods (e.g., Ensemble Kalman filter) and chose a deep learning (DL) approach instead. In our DL approach for tuning the neXtSIM parameter values, we train a neural network based on the modelling results and apply it to actual observations. The inputs for the neural network are the descriptors of the sea ice deformation, and the target is a value of a rheological parameter.

The algorithm for DL parameter tuning can be summarised as follows:

1. We choose the neXtSIM rheology parameters for tuning and perturb their values to generate an ensemble. Let $\phi_{m,n}$ denote the m-th parameter for the n-th member of the ensemble, then ϕ_m denotes a vector of the m-th parameter for all members.

115   2. An ensemble of neXtSIM instances is run with the same forcings but with different rheology parameters:

$$\tilde{\boldsymbol{x}}_{n,t+1} = \mathcal{M}(t, \tilde{\boldsymbol{x}}_{n,t}; \boldsymbol{\phi}_n), \tag{9}$$

where $\tilde{\boldsymbol{x}}$ is the sea ice model state (e.g., sea ice concentration, thickness, drift, etc.), $\mathcal{M}$ is neXtSIM model, and t is time.

3. Let $\boldsymbol{x}$ denote only one model variable: sea ice drift. Then $\mathcal{H}$ denotes the operator for computing a sea ice deformation field and a quantitative characterisation of ice deformation pattern $\boldsymbol{y}$:

120
$$\boldsymbol{y}_{n,t} = \mathcal{H}(\boldsymbol{x}_{n,t}). \tag{10}$$

The size of $\boldsymbol{y}_{n,t}$ is much smaller than the ice deformation field. For example, a daily deformation field containing $\sim 10^{10}$ sea ice deformation values can be characterised by a vector with ~ 50 values.

4. Let $\boldsymbol{y}$ denote a set of $\boldsymbol{y}_{n,t}$ vectors from all members and all time steps. Hereafter, $\boldsymbol{y}$ is called deformation pattern descriptors, or simply, descriptors. A neural network $\mathcal{N}$ is trained (operator $\mathcal{T}$) with the deformation pattern descriptors

125   ($\boldsymbol{y}$) as input and the rheology parameters ($\boldsymbol{\phi}_m$) as the target:

$$\mathcal{N}_m = \mathcal{T}(\boldsymbol{y}, \boldsymbol{\phi}_m). \tag{11}$$

5. Deformation fields and deformation pattern descriptors are computed from the observed sea ice drift $\boldsymbol{x}^o$ for each time step t:

$$\boldsymbol{y}_t^o = \mathcal{F}(\boldsymbol{x}_t^o). \tag{12}$$

130   6. The neural network is applied to the deformation pattern descriptors computed from the observed ice drift, and averaging ($\langle\rangle$) is applied for computing the optimal value of a neXtSIM parameter:

$$\begin{aligned} \boldsymbol{\phi}_{m,t}^o &= \mathcal{N}_m(\boldsymbol{y}_t^o) \\ \boldsymbol{\phi}_m^o &= \langle \boldsymbol{\phi}_{m,t}^o \rangle. \end{aligned} \tag{13}$$

All these steps are described in detail below.

4.2   Running an ensemble of neXtSIM instances

135   We ran two ensembles with neXtSIM instances. In the first experiment, the ensemble consisted of 50 members and the values of four parameters were perturbed using Latin Hypercube (see Table 1 for reference): P_0, c_{ref}, ν and μ. In the second experiment with 70 members, the following parameters were perturbed: P_0, c_{ref}, H, A and C_a. See the distribution of the perturbed parameters in Figure 3.

   NeXtSIM instances were run at 10 km resolution mesh, covering the central Arctic Ocean. Ocean forcing from TOPAZ4

140   reanalysis (Sakov et al., 2012) and atmosphere forcing from ERA5 reanalysis (Hersbach et al., 2020) were used. NeXtSIM
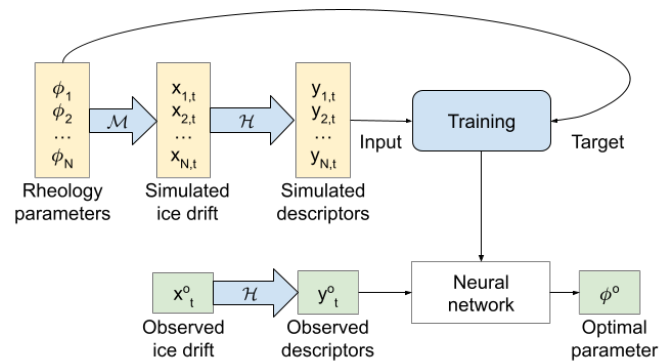
Figure 2. Scheme of ML-based tuning of neXtSIM parameters. Blue arrows denote operations with data. Yellow squares denote modelling data. Green squares denote observations.
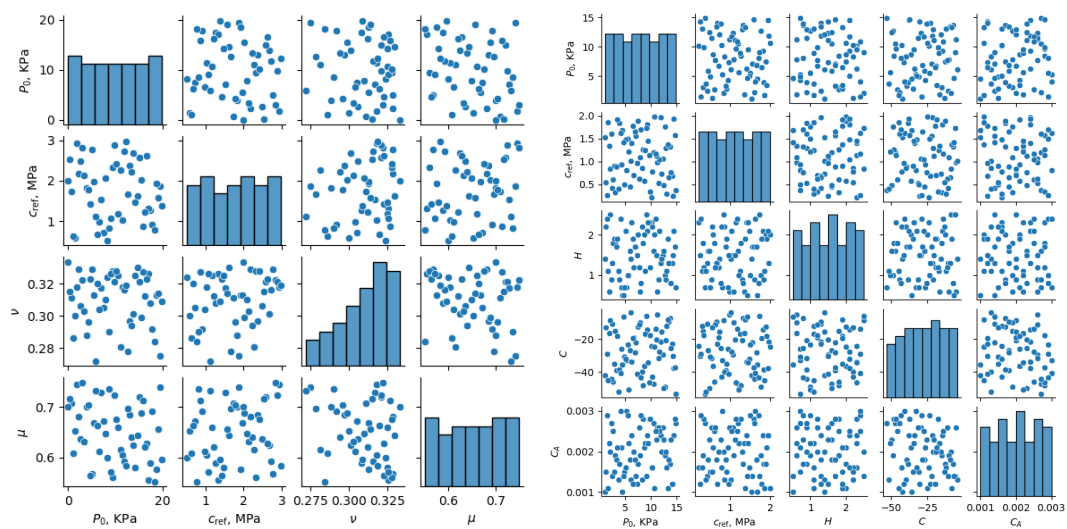
Figure 3. Values of neXtSIM parameters perturbed in two experiments.
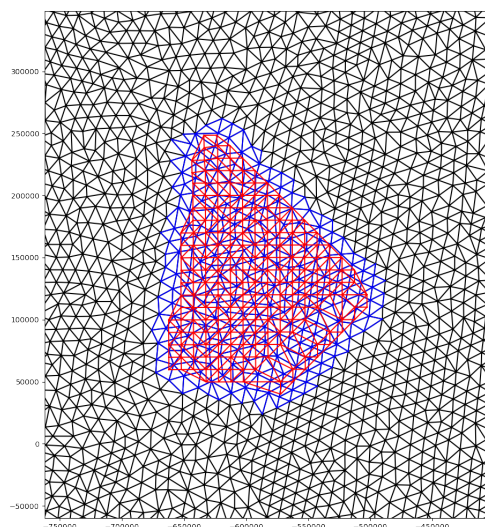
Figure 4. Illustration of RGPS and neXtSIM mesh collocation. The neXtSIM mesh from one snapshot is shown in black. The RGPS mesh created by triangulation of virtual drifters detected on a pair of Radarsat-2 images is shown in red. The neXtSIM mesh subsampled from the original mesh for collocation with the RGPS mesh is shown in blue.

exports snapshot outputs every hour with coordinates and connectivity of the nodes of the triangular mesh and model variables for each mesh element, including ice concentration, thickness, etc. End-to-end indexing of the model nodes allows the identification of similar nodes on two snapshots and the computation of the displacement of the node, i.e., the simulated sea ice drift.

4.3 Preprocessing of neXtSIM data

To ensure comparability of sea ice drift and deformation from RGPS and neXtSIM, we subsample the model mesh using the mesh of satellite observations. First, for a given set of virtual RGPS buoys that have the same starting time and ending time (i.e., a single pair of SAR images is used for ice drift computation for these buoys), two model snapshots with the closest simulation time are selected from the neXtSIM outputs. Next, only the neXtSIM nodes near the RGPS nodes are selected on the first snapshot, and the corresponding nodes are chosen on the second snapshot (see Figure 4 for an example). Nodes may disappear during simulation, or new nodes appear due to convergence/divergence and consequent remeshing. In that case, a new Delaunay triangulation connectivity is computed between the nodes existing on the first and the second snapshots. Further drift, deformation, and descriptor calculations are performed on subsets of trajectories (same for RGPS or neXtSIM) with the same start and end time and are somewhat limited in space (by the intersection area of two SAR images).

4.4 Computing the descriptors of the sea ice deformation

We compute the divergence and shear components of the deformation tensor and the total deformation rates using a standard method of contour integrals of velocity (Kwok, 2006) for each element of the mesh subset mentioned above. The following descriptors of the total deformation field are computed from each subset as described in the subsections below:

1. Structure-function from the spatial scaling analysis

2. Image anisotropy at different spatial scales

3. Haralick texture features at different spatial scales

4. Length, density and angle of intersection of linear kinematic features (LKFs)

5. Mean and 90th percentile of ice deformation values

4.4.1 Spatial scaling analysis

As described in Ólason et al. (2022), the deformation is computed at different spatial scales by iterative coarse-graining (Marsan and Weiss, 2010). First, the deformation is computed on the native resolution of RGPS and neXtSIM (which are very similar). Next, some nodes are randomly removed, the remaining node positions are triangulated, and deformation is computed again. The last step is repeated several times until at least three nodes remain in the subset. Information about the area of the element used for computing deformation is preserved. This iterative procedure is repeated several times, starting from the initial deformation field to collect sufficient deformation observations computed at different spatial scales.

The spatial scale L is linked with the statistical moments Q of the total deformation probability density function using the following equation:

$$L_{lg} = \alpha_N + \beta_N Q_{lg}^N, \tag{14}$$

where α and β are coefficients found using the least squares method, N is the statistical moment order, and the subscript lg indicates logarithmic space. The N-th statistical moment is computed as $Q_{lg}^N = \langle \log_{10}((\varepsilon - \hat{\varepsilon})^N) \rangle$, where $\hat{\varepsilon}$ is mean total deformation and $\langle \rangle$ denotes averaging.

Coarse graining is performed on each deformation subset (see Section 3.3). Still, the α and β coefficients are computed using deformation values (and corresponding spatial scales) from all image pairs acquired within three days. Hereafter, the offset and scale of the 1st statistical moment is denoted `mom_1o` and `mom_1s`, and so on (see Table 2).

4.4.2 Image anisotropy

Image anisotropy a_I characterises localisation of image intensity in a linear feature (Lehoucq et al., 2015). Anisotropy is high (up to 1) for images of bright, narrow, long lines and is low (down to 0) for images with darker, shorter or thicker lines. We
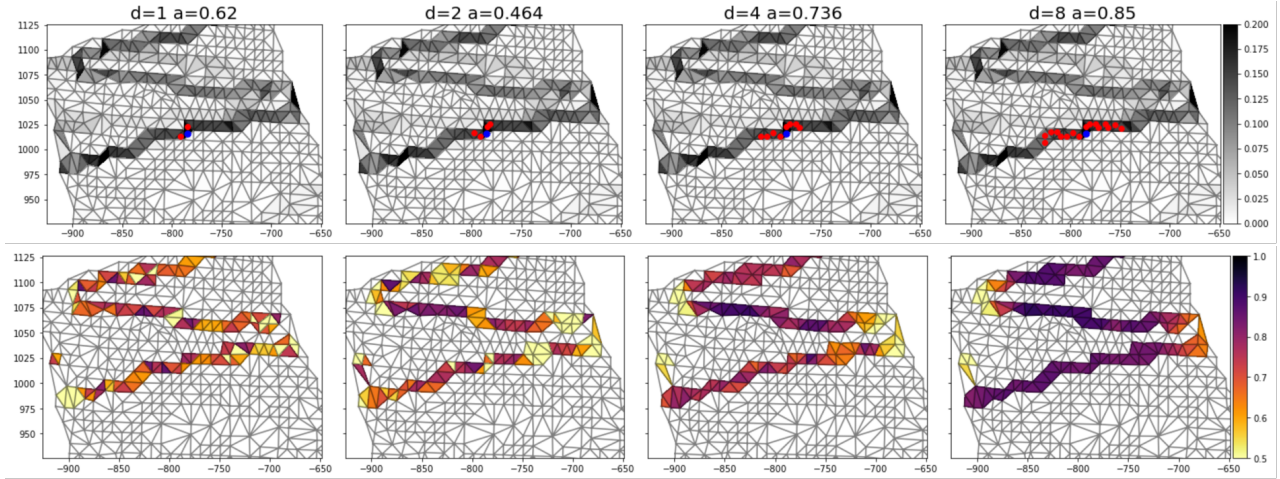
Figure 5. Computation of image anisotropy on a mesh subset. The upper row shows a mesh subset with values of ice deformation (d^{-1}), and the lower row - values of anisotropy computed at different spatial scales. The blue dot on the upper row shows the location of an arbitrary element for which anisotropy is computed, and the red dots show the neighbours from which the deformation and coordinates are collected.

compute the image anisotropy as:

$$a_I = 1 - \sqrt{\frac{\lambda_1}{\lambda_2}} \tag{15}$$

185 where λ_1, and λ_1 are the eigenvalues of the inertia matrix $\mathbf{P}$:

$$\mathbf{P} = \sum_{box} \begin{pmatrix} X^2 & XY \\ XY & Y^2 \end{pmatrix} I \tag{16}$$

where X and Y are coordinates of the pixels of the image with intensities I (i.e. ice deformation in our case).

In our study, anisotropy is computed on triangular mesh elements as illustrated in Fig. 5. Only elements with deformation above 0.1 d^{-1} are used to avoid the impact of noise in sea ice drift and deformation (Dierking et al., 2020). For computing a_I

190 in a selected element, the nearest neighbour elements are found, and values of deformation and the coordinates of the centres of the elements are used in Eqs. 15 and 16 (see Fig. 5, left column). For larger spatial scales (Fig. 5, 2nd, 3rd and 4th columns), values of the deformation and coordinates are collected from the neighbours of the neighbours. After processing a single mesh subset, each element is characterised by a vector of image anisotropy computed at spatial scales of 10, 20, 30, 40 and 50 km. For every three days, a median and P90 of anisotropy from all elements of all mesh subsets are computed for each spatial scale

195 and denoted hereafter as `a50_00`, `a90_00` and so on (see Table 2).

4.4.3 Texture features

Haralick texture features (TF) are extensively used for quantitative characterisation of image texture in tasks dealing with image segmentation (Haralick et al., 1973; Zakhvatkina et al., 2017; Park et al., 2019). A grey-level co-occurrence matrix (GLCM)
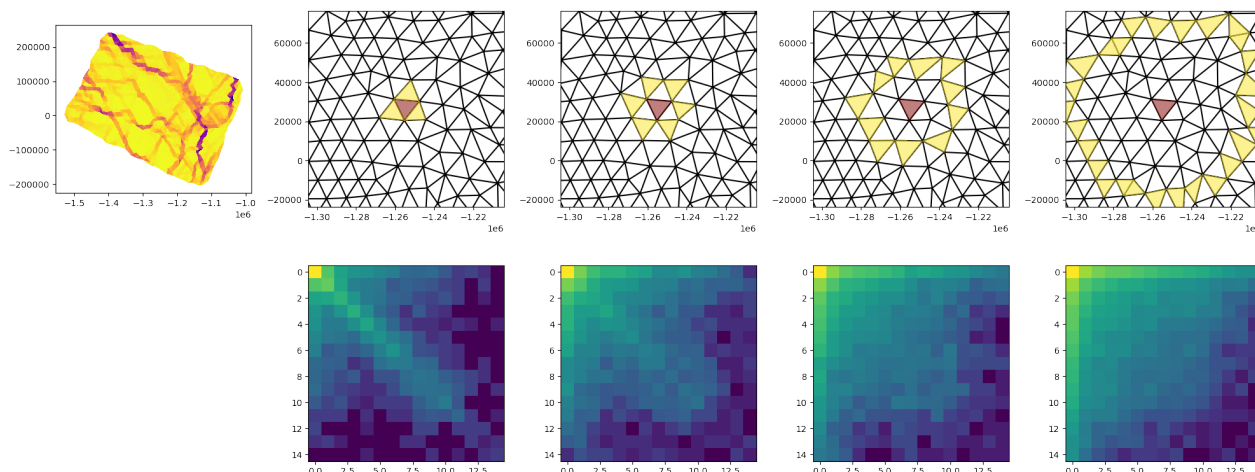
Figure 6. Scheme of GLCM computation. The upper left map shows a mesh subset with values of total deformation from neXtSIM. The upper row shows neXtSIM mesh with the central element coloured orange, and the neighbours at the one, two, four, and eight edge distances are coloured yellow. The lower row of images shows corresponding GLCM matrices.

is computed at the first stage of the texture analysis. GLCM is a 2D distribution of the probability of a pixel value and its

200 neighbour value. The neighbours can be selected at varying orientations and distances from the central pixel. At the second stage of texture analysis, several simple algebraic formulas are applied to the GLCM to compute statistical moments of the distribution (e.g., mean, standard deviation, kurtosis, etc.) and more complex characteristics (energy, entropy, etc.)

In our study, we compute the GLCM from the elements of the triangular mesh. We accumulate information about an element and all its neighbours at a given distance in all directions in one GLCM. For one–edge distance, we use the values from

205 three immediate neighbours; for two–edge distances, we use the values from neighbours of neighbours (excluding the central element and duplication), and so on, as shown in Fig. 6. We populate the GLCM matrix with data from all elements from all mesh subsets acquired within three days. The following texture features (TFs) are computed at distances of 1, 2, 4, and 8 edges using the `scikit-image` Python library (van der Walt et al., 2014): Dissimilarity, Homogeneity, Angular Second Moment, Energy, Correlation, Contrast. For notation, see Table 2. Zakhvatkina et al. (2017) provides the exact formulas.

210 ### 4.4.4 LKF intersection angle

Hutter et al. (2019) proposed a method for detecting linear kinematic features (LKFs) on RGPS and model data and several metrics for the characterisation of LKFs. These metrics are successfully applied to evaluate sea ice models in a large intercomparison experiment (Hutter and Losch, 2020). In our work, we rasterised the 3-day deformation maps on 12.5 km resolution grids and applied the LKF detection method of Hutter et al. (2019). The number of LKFs, average length of LKFs, and average

215 intersection angle of conjugate faults were used as the descriptors (see Table 2 for notations).

Table 2. Descriptors notation.

Description	Notation
Divergence, Convergence and Shear median and P90	`div_50, div_90, cnv_50, cnv_90, she_50, she_90`
Anisotropy median at 10, 20, 30, 40 and 50 km spatial scale	`a50_00, a50_05, a50_10, a50_15, a50_20`
Anisotropy P90 at 10, 20, 30, 40 and 50 km spatial scale	`a90_00, a90_05, a90_10, a90_15, a90_20`
Dissimilarity TF at a distance of 1, 2, 4, 8 pix	`dis_01, dis_02, dis_04, dis_05`
Homogeneity TF at a distance of 1, 2, 4, 8 pix	`hom_01, hom_02, hom_04, hom_05`
Angular Second Moment TF at a distance of 1, 2, 4, 8 pix	`asm_01, asm_02, asm_04, asm_05`
Energy TF at a distance of 1, 2, 4, 8 pix	`ene_01, ene_02, ene_04, ene_05`
Correlation TF at a distance of 1, 2, 4, 8 pix	`cor_01, cor_02, cor_04, cor_05`
Contrast TF at distances of 1, 2, 4, 8 pix	`con_01, con_02, con_04, con_05`
1ˢᵗ, 2ⁿᵈ and 3ʳᵈ statistical moment slope and offset	`mom_1s, mom_2s, mom_3s, mom_1o, mom_2o, mom_3o`
Average LKF intersection angle, length and number	`lkf_an, lkf_ln, lkf_no`

In addition to the descriptors listed above, the mean and P90 of divergence, convergence and shear were computed for each of the three days. Thus, a vector of descriptors constituted 49 values: mean and P90 of deformation; mean and P90 of image anisotropy computed at five spatial scales; 6 texture features at four distances; slopes and offsets of 3 statistical moments; length, number and intersection of LKFs. Table 2 shows the notation used hereafter in detail. Such vectors were generated

220 from neXtSIM simulations for each day (using a sliding window of 3 days) from 5 December 2006 to 11 April 2007 for the first experiment and from 5 December to 15 May for the second experiment. Therefore, we had $127 \times 50 = 6350$ and $161 \times 70 = 11270$ vectors for training the ML model in the first and the second experiments.

4.5 Selection of usable descriptors

We test the applicability of these descriptors using two methods: comparison of PDFs for descriptors from RGPS and neXtSIM

225 on the one hand and using an autoencoder on the other. In the first method, we scale the values of descriptors from RGPS using the mean and standard deviation of the values from neXtSIM: $y_s = (y_o - \mu)/\sigma$, where y_o are all descriptors from RGPS, μ and σ are mean and standard deviation for all descriptors from neXtSIM.

The mean and standard deviation of the scaled descriptors are analysed, and only the descriptors with scaled standard deviation below 3 remain for further use. Other descriptors computed from RGPS data have significantly different values from

230 the neXtSIM descriptors and are expected to mislead the training.

We trained an autoencoder (Hinton and Salakhutdinov, 2006; Vincent et al., 2008) with dense layers with 32, 16, 8, 16, and 32 neurons on the down-selected descriptors from neXtSIM. Due to the bottleneck, the autoencoder acts as a nonlinear principal component analysis. It can be used for anomaly detection either in the input features (Hinton and Salakhutdinov, 2006) or in input records (Vincent et al., 2008). We applied the autoencoder to the down-selected neXtSIM and RGPS descriptors

235 and computed the root mean square difference (RMSD) between the input vector and the autoencoder output for neXtSIM

and RGPS. We excluded the descriptors with high RMSE in RGPS data from further processing as anomalous compared to
neXtSIM training data.

4.6 Training of machine learning algorithms

We trained two types of ML models with the values of deformation pattern descriptors on input and a single value of a neXtSIM

240 parameter as a target: a linear regression model (LR) and a deep neural network (DNN). For both models, we randomly split the
training dataset (from neXtSIM) into two parts (85:15) for training and validation and then applied it to all RGPS descriptors.
We repeated this procedure ten times with a new random permutation and averaged the inference results on RGPS from each
repetition. The Eqs. 11 and 13 can be rewritten as follows with i being the index of repetition:

$$\mathcal{N}_{m,i} = \mathcal{T}(\boldsymbol{y_i}, \boldsymbol{\phi}_{m,i}), \tag{17a}$$

245 $$\phi^o_{m,t,i} = \mathcal{N}_{m,i}(\boldsymbol{y}^o_t), \tag{17b}$$

$$\phi^o_m = \langle \phi^o_{m,t,i} \rangle \tag{17c}$$

The LR model can be formulated as:

$$\phi_p = A_p Y, \tag{18}$$

where ϕ_p is the vector of the p-th model parameter for all 3-day periods, Y is a matrix with down-selected descriptors for all

250 periods, and A_p is a matrix with linear regression coefficients for that model parameter. Values in A_p are found using the least
squares method. The LR model does not require a split into training/validation datasets. However, only the training dataset was
compared with the DNN results.

The DNN model contains three hidden dense layers with 32, 16, and 8 neurons. We found this architecture optimal in a
simple hyperparameter tuning experiment. We trained the DNN with the Adam optimiser, and the validation loss (computed as

255 absolute error) decreased.

5 Results and discussions

5.1 Sea ice deformation fields from neXtSIM

Ólason et al. (2022) identified P_0 and c_{ref} as two parameters of their rheology, which are poorly constrained and have a
substantial visual impact on the deformation fields. Fig. 7 compares total sea deformation derived from RGPS (first column),

260 and neXtSIM runs from the first experiments with the highest and lowest values of P_0 and c_{ref}. Three dates were chosen for Fig.
7 in 2007 with low (15 February), moderate (25 January) and high (3 February) deformation events. These maps illustrate that
both parameters significantly affect the pattern of sea ice deformation, but their influence is manifested differently. For example,
the increase of P_0 results in broader and longer LKFs with higher deformation rates. These pronounced LKFs surround quite
large floes; the background deformation remains relatively low. The increase of c_{ref} seems to affect the background deformation
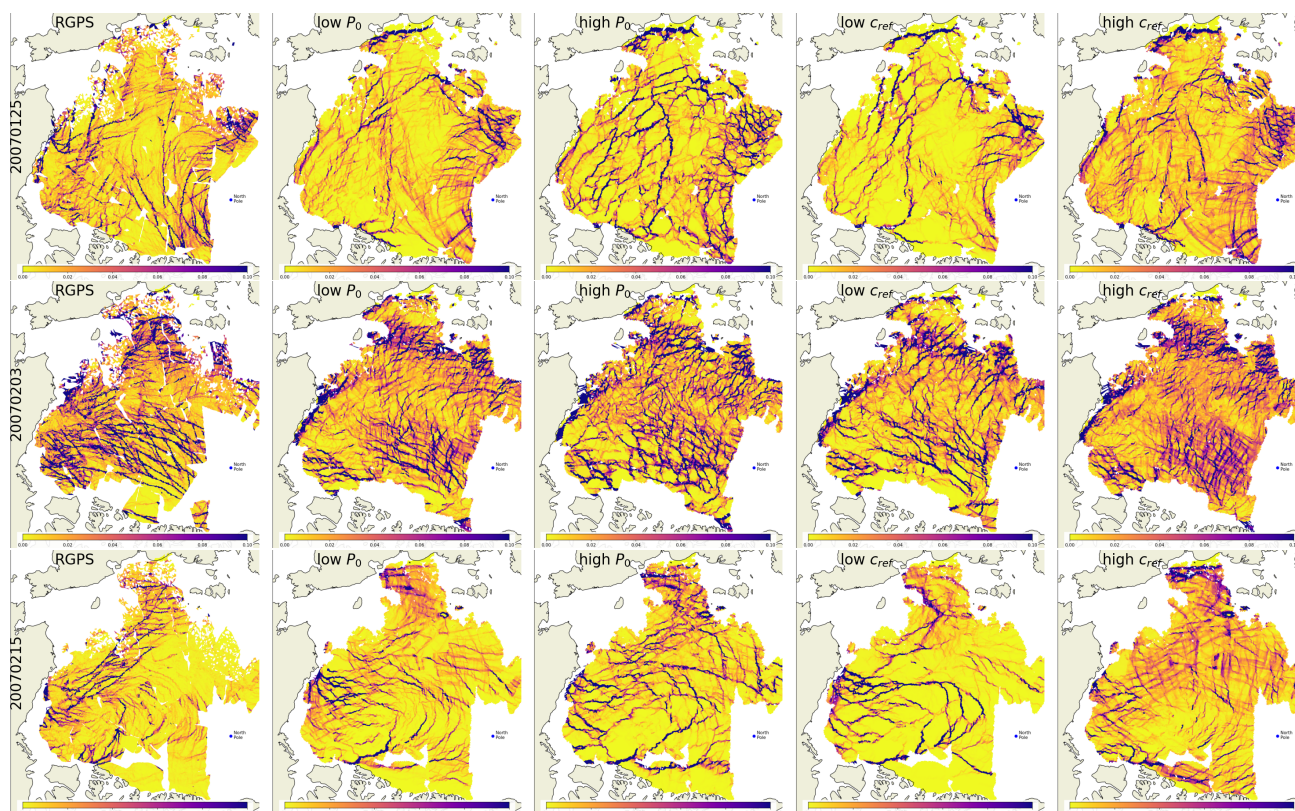
Figure 7. Maps of total deformation from RGPS and neXtSIM computed from tree days snapshots for three selected dates representing moderate, high and low deformation events.

more — at the lowest c_{ref} value, the deformation between the main LKFs is mostly zero, and it increases with higher c_{ref} to become almost spatially homogeneous. It is hard to say which of these maps better matches the RGPS data, but it is clear that optimization of multiple rheology parameters is required to find the best match.

5.2 Deformation pattern descriptors

Fig. 8 shows the PDFs of the deformation pattern descriptors computed from RGPS and the first neXtSIM experiment. Comparison of the PDFs from all neXtSIM runs (blue shaded area) with the PDFs from the run with the lowest (orange line) or the highest (green line) P_0 value illustrates that some descriptors (e.g., `a50_00`, `a90_05`, `hom_02`, `con_01-08`, etc.) are strongly affected by P_0 — their PDF peaks are distinctly different. Other descriptors (e.g., `ASM_01-08`, `a50_10`, etc.) have very similar PDFs without regard for the P_0 parameter.

The PDF of most RGPS–derived descriptors lies well within the range of neXtSIM-derived descriptors and peaks between the highest and lowest P_0 PDFs (e.g., `a90_05`, `dis_04`, `mom_3o`, etc.) suggesting that we can use these descriptors for parameter tuning. Some RGPS descriptors, however, show a completely different distribution (e.g., `hom_08`, `cor_08`, etc.),

probably due to sensitivity to noise in observations. Such descriptors are not usable for parameter training and are excluded as described in section 4.5.

Figure 9 shows the correlation of all descriptors with the values of all parameters from the first experiment. The correlations
280 are generally relatively low, except for c_{ref}, which correlates with she_50 and cor_01 above 0.35. Results from the second experiment are pretty similar. The low correlation suggests that methods for parameter estimation that rely on the linear relation between model variables and observations (e.g. Ensemble Kalman filter) are less efficient in our task.

Figure 10 presents the mean and standard deviation of the RGPS-derived descriptors normalised by the mean and standard deviation of the neXtSIM descriptors. We use it at the first step of evaluating usability and downselecting the descriptors.
285 Only 43 descriptors computed from RGPS data show the relative mean value between -1.5 and 1.5 standard deviations of the neXtSIM descriptors. We exclude the following six descriptors from further processing: cor_08, a50_08, cor_01, ene_08, dis_08, hom_08.

Fig. 11 compares root mean square difference (RMSD) between input and predictions of the autoencoder trained on normalised neXtSIM data and applied to neXtSIM and RGPS descriptors. The RMSD of neXtSIM — derived descriptors is below
290 one, showing that even a relatively shallow autoencoder (five layers with eight neurons in the bottleneck) can reproduce the variability of the descriptors well. When the same autoencoder is applied to the RGPS data, some of the descriptors (cnv_90, con_08, lkf_ln, lkf_no, a90_20, lkf_an, and a90_00) have RMSD higher than the maximum neXtSIM RMSD. High RMSD indicates abnormal values, and we exclude the corresponding descriptors from further training.

5.3 Training and inference of ML models

295 Fig. 12 shows the DNN training results for the first (upper row) and the second (lower row) experiments (see also Table 3). These scatterplots compare the actual and the predicted neXtSIM parameters from the test dataset from all ten repetitions. In the first experiment, the DNN derives only the P_0 and c_{ref} with sufficient accuracy (correlation is 0.75 and 0.88, respectively). In the second experiment, the accuracy of P_0 retrieval is somewhat lower ($r = 0.61$), while the accuracy of c_{ref} and C_A retrieval is high (correlation is 0.83 and 0.75, respectively). The DNN does not show any skill in retrieving ν or H parameters, and the
300 accuracy of retrieving μ and C is somewhat higher for a short range of values. Still, overall, these four parameters cannot be derived with the machine learning approach. LR accuracy is lower (see Table 3), and the scatterplots are not shown.

Figure 13 shows PDFs of parameters used for training (blue line) and derived from the RGPS data using DNN (orange line) and LR (green line) models in the two experiments mentioned above (upper and lower row). In both experiments, PDFs of P_0 and c_{ref} parameters have a clear peak at ≈5000 kPa and ≈1.1 MPa, correspondingly. Notably, these peaks do not correspond
305 to the centre of the distribution of the parameters used for training (blue line). We can observe similar behaviour for μ and C_A parameters, which also have relatively high retrieval accuracy of testing data. For ν, H, and C parameters, the situation is different — the accuracy of the retrievals on the testing data was low, and the retrievals from the RGPS data are centred in the distribution of training values.
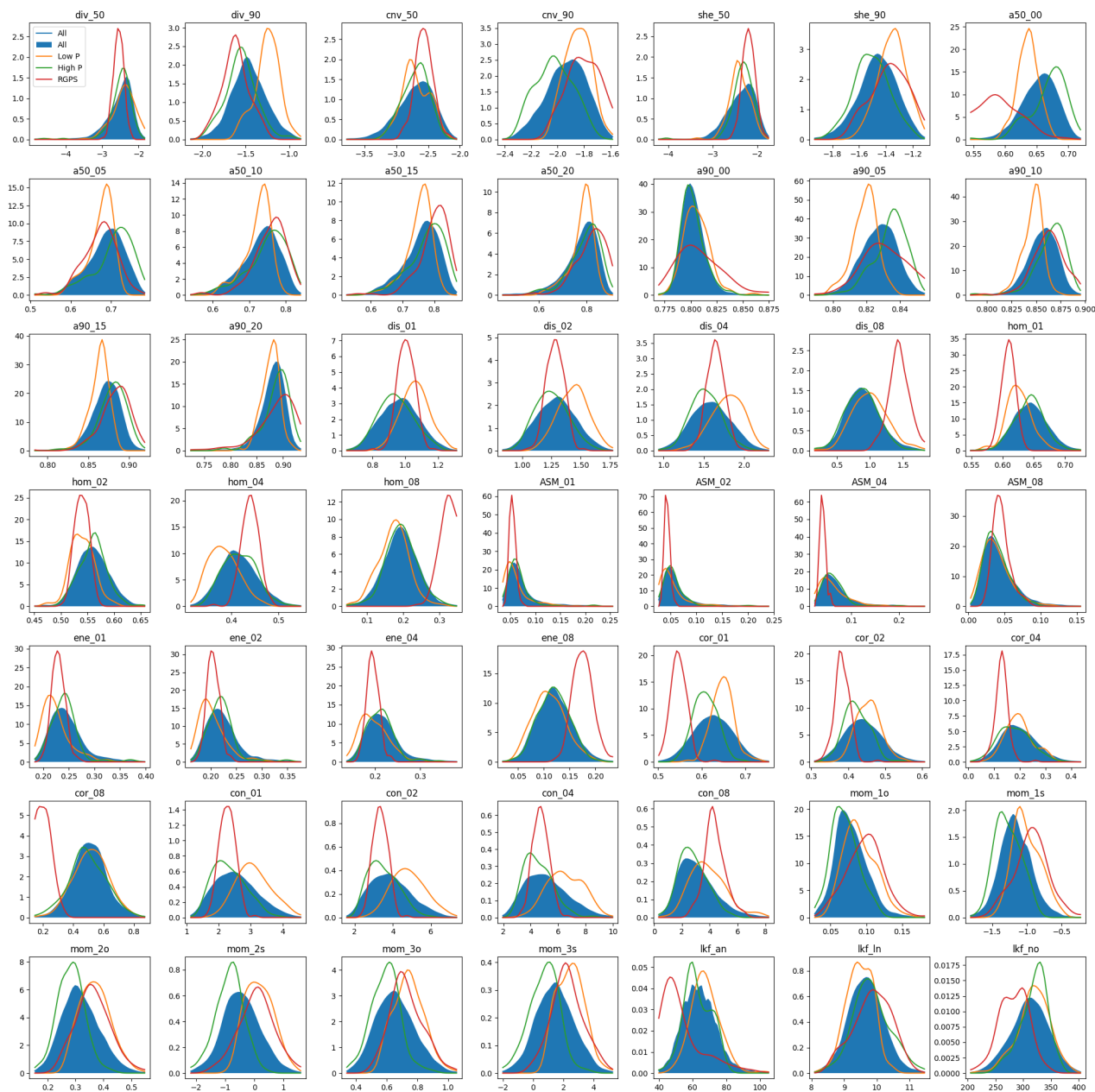
Figure 8. PDFs of all deformation descriptors for RGPS (red), all neXtSIM runs (blue), and runs with lowest (orange) or highest values of P_0.
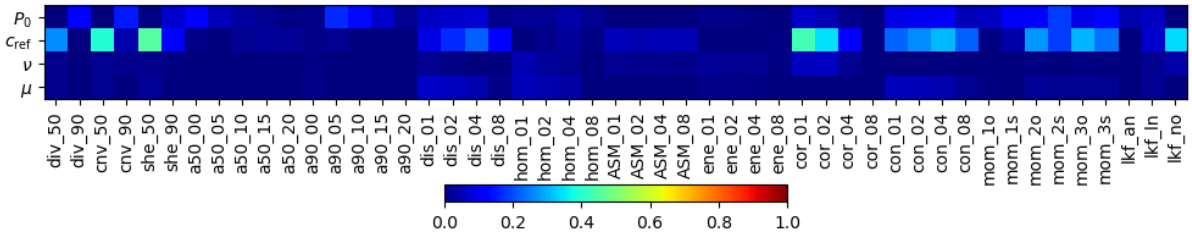
Figure 9. Correlations between four parameters of the first experiment and the deformation descriptors.
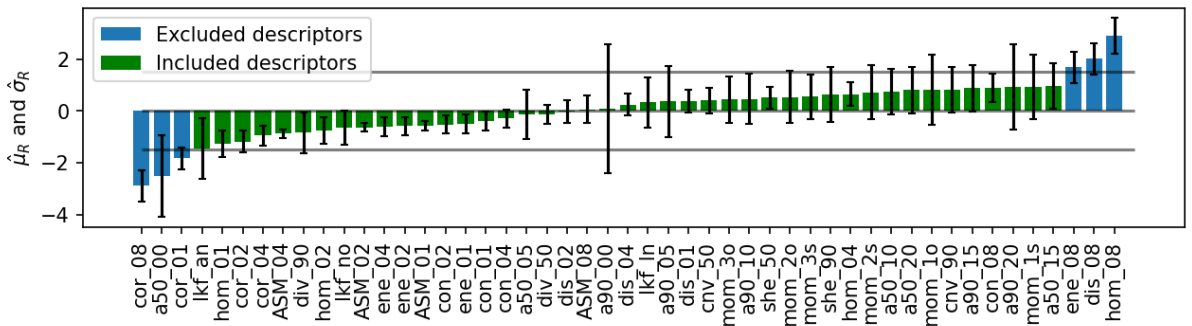
Figure 10. Relative values of the mean and standard deviation of descriptors computed from RGPS data. The blue colour shows the excluded descriptors.
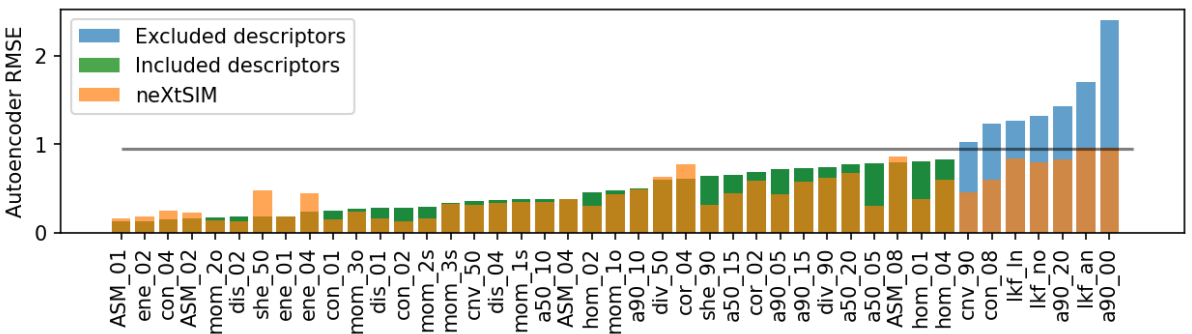
Figure 11. RMSD between input and output of the autoencoder trained on neXtSIM data and applied to neXtSIM (orange) and RGPS (blue or green). The blue colour shows RGPS descriptors excluded from further analysis.
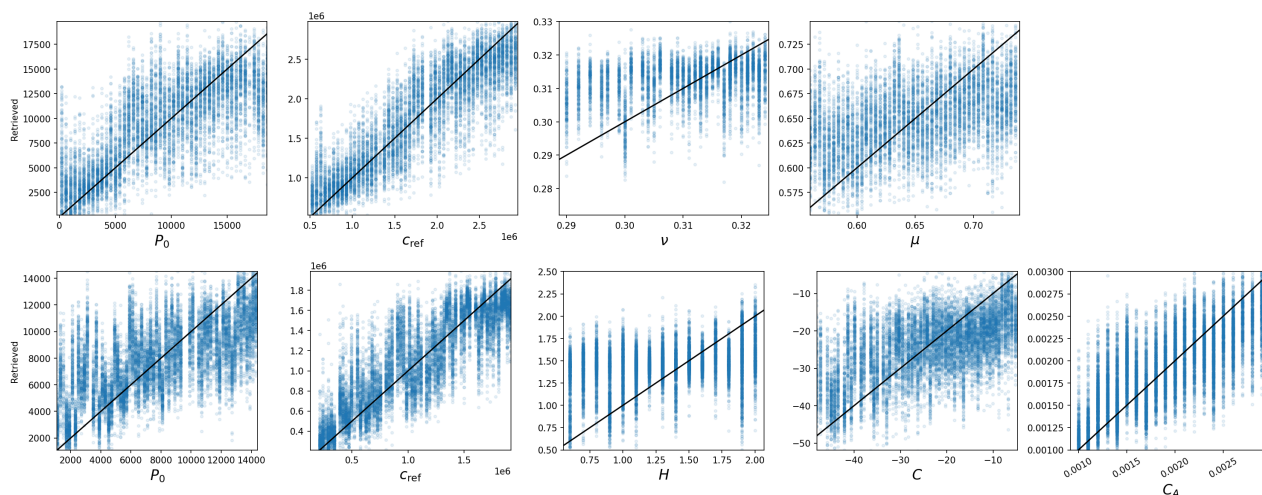
Figure 12. Comparison of the actual neXtSIM parameters (X-axis) and the retrievals by the DNN. The upper row shows results from the first experiment, and the lower — the second one.
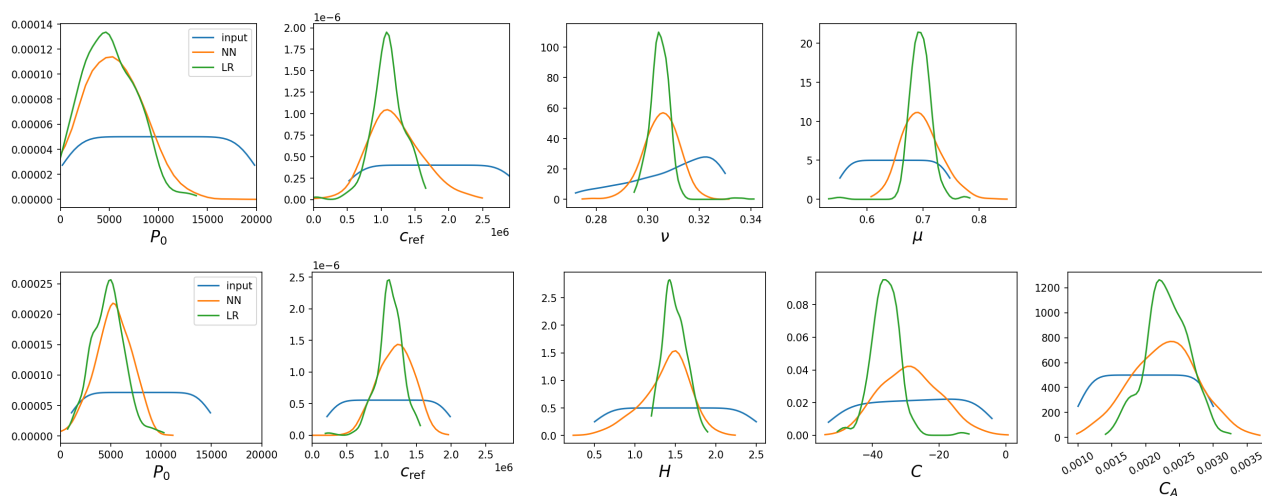
Figure 13. PDFs of parameters used for training (blue lines) and derived from RGPS descriptors using DNN (orange) and LR (green). The upper row shows the results from the first experiment, and the lower — the second.

Table 3. Average values of neXtSIM parameters derived from RGPS. The optimal values are marked in bold.

Param	Exp	Method	r training	Mean inference
P_0	1	LR	0.66	4.88 kPa
P_0	1	NN	0.75	**5.11 kPa**
c_{ref}	1	LR	0.83	1.10 MPa
c_{ref}	1	NN	0.88	**1.21 MPa**
ν	1	LR	0.36	0.305
ν	1	NN	0.35	0.305
μ	1	LR	0.4	0.70
μ	1	NN	0.5	**0.70**
P_0	2	LR	0.59	4.72 kPa
P_0	2	NN	0.61	5.26 kPa
c_{ref}	2	LR	0.78	1.11 MPa
c_{ref}	2	NN	0.83	1.19 MPa
H	2	LR	0.3	1.49
H	2	NN	0.35	1.38
C	2	LR	0.47	-36.1
C	2	NN	0.54	-28.7
C_A	2	LR	0.69	2.32×10^{-3}
C_A	2	NN	0.75	**2.28×10^{-3}**

5.4 Optimal rheology parameters for neXtSIM

310 Since the training accuracy was high, the peaks of PDFs of RGPS-derived parameters are pronounced and have offset from the centre of the input data distribution; we can conclude that the values of P_0, c_{ref}, μ and C_A parameters derived from RGPS can be used for optimal representation of the deformation patterns by neXtSIM. Table 3 lists the parameter values derived in different experiments and the accuracy of the model training. Note that DNN always has higher accuracy than the LR model.

We ran neXtSIM with the optimal parameter values, and Figure 14 shows a comparison with RGPS for the exact three 315 dates. We can see that the patterns of the divergence and shear fields are very similar for neXtSIM and RGPS with regard to the density and orientation of LKFs, the magnitude of deformation, and, overall, the texture of the deformation field, thus confirming that the found parameters are indeed optimal.

It is interesting to note similarities and differences between the parameters used by Ólason et al. (2022). We note that the values we get for ν, μ, and H are very similar to those Ólason et al. (2022) used. This is to be expected for ν and μ, which 320 are based on well established values (see, e.g. Weiss and Schulson, 2009; Mellor, 1986). Ólason et al. (2022) chose $H = 3/2$

based on the modelling work of Hopkins (1998), but it is unclear whether this should be valid at the geophysical scale. The accuracy of our estimate for H is low, but it is reasonably close to $H = 3/2$ and within the expected range of $H \in [1, 2]$.

In terms of the stress balance in the ice, C_A, P_0, and c_{ref} are the most important, as they determine the momentum transfer from atmosphere to ice, the resistance to ridging, and the shear strength of the ice, respectively. Interestingly, our estimate of C_A is higher than the value used by Ólason et al. (2022); 2.28×10^{-3} vs. 2.0×10^{-3}, resulting in more momentum transfer from the atmosphere to the ice. At the same time, both P_0 and c_{ref} are lower; 5.11 kPa vs. 10.0 kPa and 1.21 MPa vs. 2.0 MPa, respectively. This results in an overall weaker ice cover compared to the parameters used by Ólason et al. (2022). It would, therefore, be reasonable to expect that our set of parameters would lead to an overestimate of the deformation, but this is not the case. This underlines the system's complexity and indicates that there may be multiple local minima in the parameter space, giving reasonable results. For such a system, using a systematic approach which samples the full parameter space - similar to what we propose here - is extremely beneficial.

5.5 Temporal variations of neXtSIM parameter values

The PDFs of parameters presented in Figure 13 are derived from all RGPS descriptors computed in winter 2006–2007. Figure 15 shows temporal variations of the derived optimal parameters on daily and inter-annual time scales. To create the latter plot, we computed the descriptors from the RGPS data for 1997–2008 and applied the DNN models trained on neXtSIM data from 2006–2007.

On daily time scales, the derived parameters show very high variability, reflecting frequent changes in the pattern of sea ice deformation due to varying atmospheric forcing. The DNN model from the first experiment is more sensitive to these variations and even produces unphysical negative values during very high deformation at the beginning of February 2007. Despite substantial variability, the parameters are stable on the annual scale and don't show any significant trends.

On the interannual scale, the parameters tend to change; P_0 and μ slightly decrease, while c_{ref} and A_C gradually increase. A gradual change in the observed pattern of sea ice deformation can explain this observation. In the 90s, thicker ice had sparser and more pronounced LKFs (see Fig. 7, high P_0 and low c_{ref} maps). As ice became thinner, more background deformation appeared, LKFs became denser, and the magnitude of deformation in LKFs slightly decreased (see Fig. 7, low P_0 and high c_{ref} maps). The impact of internal friction angle or air drag is not shown in Figure 7, but the mechanisms are similar: higher Mohr-Coulomb slope allows the ice to resist breakup longer and creates larger floes (mimicking earlier, thicker ice situation); low air coefficient decreases ice drift and, consequently, ice deformation which again corresponds to an earlier period of RGPS observations.

After the first experiments, we observed the interannual trends in the P_0 and c_{ref} parameters. This leads us to conclude that the weak dependence of these rheology parameters on ice thickness (and potentially concentration) indicates that the parameterisation of P_{max} (see Eq. 2) requires better values of H and C parameters. That was the motivation to run the second experiment and to retrieve values of H, C and C_A. Unfortunately, as table 3 shows, the accuracy of ML models for these parameters is not sufficiently high, and we cannot derive their optimal values. Nevertheless, accounting for these parameters in the second experiment allowed us to train ML models that show fewer diurnal variations and are more stable on interannual
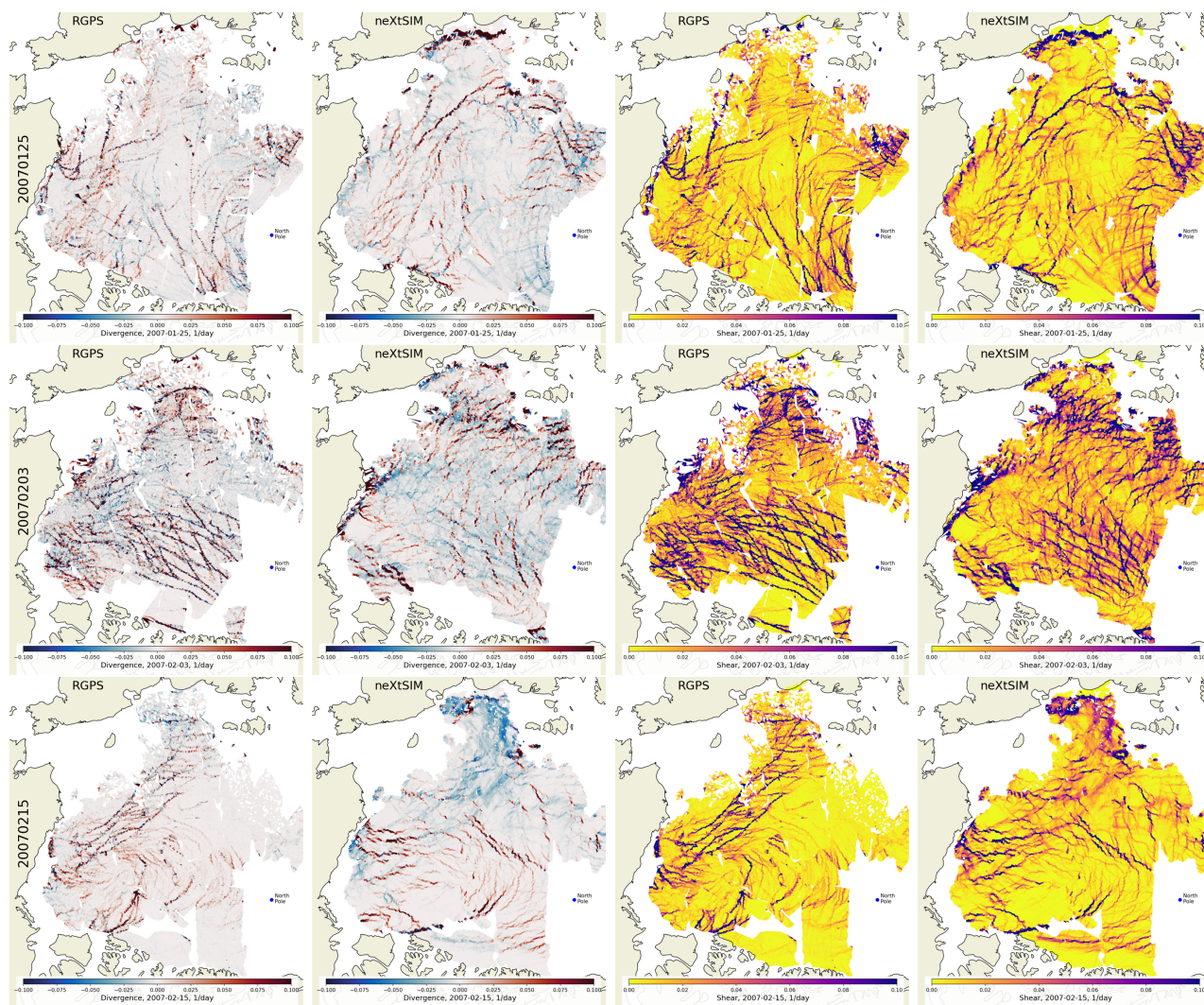
Figure 14. Maps of divergence and shear from RGPS and neXtSIM run with optimal parameters for the same dates as in Figure 7.
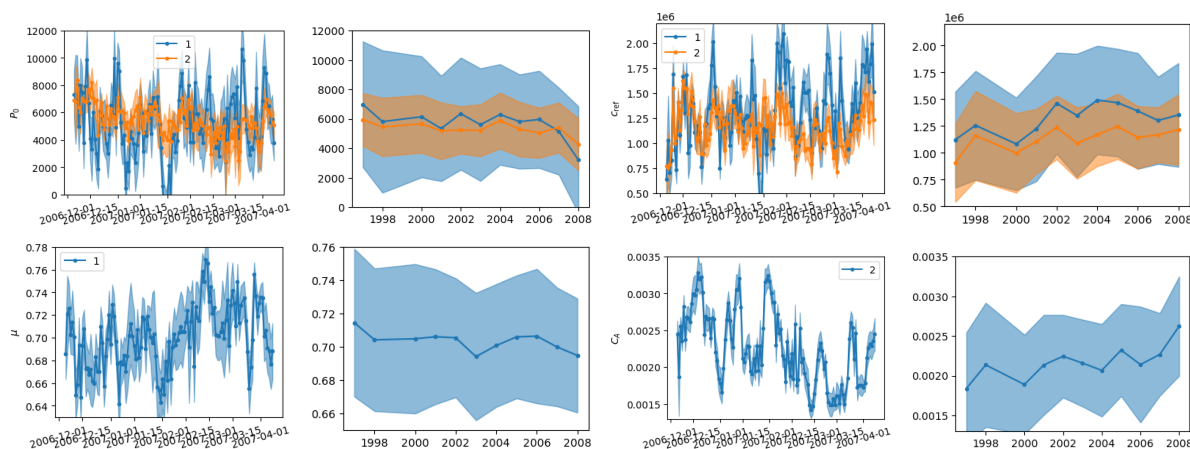
Figure 15. Time series of parameter values derived from RGPS for one year (left column) and several years (right column). Colour denotes the experiment, and the shaded area shows the standard deviation of samples produced by ten neural networks for the daily values (left column) or the samples collected from the entire year (right column).

time scales. Moreover, despite low accuracy, the ML models predict lower values of H (1.38) and C (-28.7) than the default ones. Dedicated experiments are needed to tune these parameters further.

6 Conclusions

We developed a new set of metrics for characterising the patterns in the sea ice deformation fields. These metrics are sensitive to the parameters of a sea ice model rheology and can be used to compare simulated and observed ice deformation for model evaluation or parameter tuning.

We developed a new method for tuning model parameters using machine learning. In our process, we train an ML model using simulated data and apply it to observations. In our case, the inputs to the ML model are the descriptors of sea ice deformation, and the targets are the sea ice rheology parameters. We tested a linear regression (LR) and a deep neural network (DNN) as ML models, and DNN always showed higher accuracy. This method can be applied to tune the parameters of any other model.

Using the new set of metrics and the new ML-based method, we found values of four BBM rheology parameters that were poorly constrained previously: scaling parameter for ridging ($P_0 \approx 5.1$ kPa), cohesion at the reference scale ($c_{\text{ref}} \approx 1.2$ MPa), internal friction angle tangent ($\mu \approx 0.7$), ice–atmosphere drag coefficient ($C_A \approx 0.00228$).

These parameters exhibit weak interannual drift related to changes in sea ice thickness and corresponding changes in ice deformation patterns. Improving the dependence on thickness and concentration in the BBM rheology or tuning the corresponding parameters may reduce the drift and make the rheology completely independent of ice thickness influence. Recent

observations of ice drift and deformation obtained from Sentinel-1 SAR data processing are recommended for tuning the rheology to reflect the current situation and provide higher accuracy forecasts.

Other parameters in our experiments (exponent of compression factor, Poisson's ratio, compaction parameter) did not impact
375   the pattern of sea ice deformation, or the influence of other parameters masked their impact. Therefore, their values could not be derived using our method. Dedicated experiments are required to study the sensitivity of the proposed metrics to these parameters and to tune their values.

Code and data availability. The code for processing RGPS and neXtSIM data and computing ice deformation descriptors is publicly available on GitHub (Korosov, 2024c).

380   The code for tuning the neXtSIM BBM parameters and preparation of the figures for the manuscript is publicly available on GitHub (Korosov, 2024b).

Samples of neXtSIM data used in the study are publicly available on Zenodo (Korosov, 2024a).

RGPS data is publicly available on the Alaska Satellite Facility: https://asf.alaska.edu/datasets/daac/sea-ice-measures/.

Author contributions. AK, YY and EO designed the experiment and wrote the manuscript. EO developed the BBM rheology and largely
385   contributed to the development of the netXSIM. AK developed the code for computing the metrics and running the ML-based parameter tuning. AK ran all the experiments.

Competing interests. The authors declare that no competing interests are present.

Acknowledgements. We acknowledge the support from the Research Council of Norway (project "Multi-scale Sea Ice Code", no. 325292) and the support from the Norwegian Space Agency (project "Synergy of SAR, radiometry, and altimetry for Digital Arctic Sea Ice Twin",
390   no. 74CO2221). We are thankful to Pierre Rampal for fruitful discussions of methodology for image anisotropy computation and the results of the experiments.

References

Bouillon, S. and Rampal, P.: Presentation of the dynamical core of neXtSIM, a new sea ice model, Ocean Modelling, 91, 23–37, https://doi.org/10.1016/j.ocemod.2015.04.005, 2015.

Boutin, G., Williams, T., Horvat, C., and Brodeau, L.: Modelling the Arctic wave-affected marginal ice zone: a comparison with ICESat-2 observations, Philosophical Transactions of the Royal Society A: Mathematical, Physical and Engineering Sciences, 380, https://doi.org/10.1098/rsta.2021.0262, 2022.

Boutin, G., Ólason, E., Rampal, P., Regan, H., Lique, C., Talandier, C., Brodeau, L., and Ricker, R.: Arctic sea ice mass balance in a new coupled ice–ocean model using a brittle rheology framework, The Cryosphere, 17, 617–638, https://doi.org/10.5194/tc-17-617-2023, 2023.

Brodeau, L., Rampal, P., Òlason, E., and Dansereau, V.: Implementation of a brittle sea-ice rheology in an Eulerian, finite-difference, C-grid modeling framework: Impact on the simulated deformation of sea-ice in the Arctic, Geoscientific Model Development Discussions, 2024, 1–46, https://doi.org/10.5194/gmd-2023-231, 2024.

Dansereau, V., Weiss, J., Saramito, P., and Lattes, P.: A Maxwell elasto-brittle rheology for sea ice modelling, Cryosphere, 10, 1339–1359, https://doi.org/10.5194/tc-10-1339-2016, 2016.

Dierking, W., Stern, H. L., and Hutchings, J. K.: Estimating statistical errors in retrievals of ice velocity and deformation parameters from satellite images and buoy arrays, The Cryosphere, 14, 2999–3016, https://doi.org/10.5194/tc-14-2999-2020, 2020.

Girard, L., Bouillon, S., Weiss, J., Amitrano, D., Fichefet, T., and Legat, V.: A new modeling framework for sea-ice mechanics based on elasto-brittle rheology, Annals of Glaciology, 52, 123–132, https://doi.org/10.3189/172756411795931499, 2011.

Haralick, R. M., Shanmugam, K., and Dinstein, I.: Textural Features for Image Classification, IEEE Transactions on Systems, Man, and Cybernetics, SMC-3, 610–621, https://doi.org/10.1109/TSMC.1973.4309314, 1973.

Hersbach, H., Bell, B., Berrisford, P., Hirahara, S., Horányi, A., Muñoz-Sabater, J., Nicolas, J., Peubey, C., Radu, R., Schepers, D., Simmons, A., Soci, C., Abdalla, S., Abellan, X., Balsamo, G., Bechtold, P., Biavati, G., Bidlot, J., Bonavita, M., De Chiara, G., Dahlgren, P., Dee, D., Diamantakis, M., Dragani, R., Flemming, J., Forbes, R., Fuentes, M., Geer, A., Haimberger, L., Healy, S., Hogan, R. J., Hólm, E., Janisková, M., Keeley, S., Laloyaux, P., Lopez, P., Lupu, C., Radnoti, G., de Rosnay, P., Rozum, I., Vamborg, F., Villaume, S., and Thépaut, J.-N.: The ERA5 global reanalysis, Quarterly Journal of the Royal Meteorological Society, 146, 1999–2049, https://doi.org/10.1002/qj.3803, 2020.

Hibler, W. D.: A dynamic thermodynamic sea ice model, Journal of Physical Oceanography, 9, 815–846, https://doi.org/10.1175/1520-0485(1979)009<0815:adtsim>2.0.co;2, 1979.

Hinton, G. E. and Salakhutdinov, R. R.: Reducing the Dimensionality of Data with Neural Networks, Science, 313, 504–507, https://doi.org/10.1126/science.1127647, 2006.

Hopkins, M. A.: Four stages of pressure ridging, Journal of Geophysical Research: Oceans, 103, 21 883–21 891, https://doi.org/10.1029/98JC01257, 1998.

Hutter, N. and Losch, M.: Feature-based comparison of sea ice deformation in lead-permitting sea ice simulations, The Cryosphere, 14, 93–113, https://doi.org/10.5194/tc-14-93-2020, 2020.

Hutter, N., Zampieri, L., and Losch, M.: Leads and ridges in Arctic sea ice from RGPS data and a new tracking algorithm, The Cryosphere, 13, 627–645, https://doi.org/10.5194/tc-13-627-2019, 2019.

Korosov, A.: Outputs of the next generation sea ice model (neXtSIM) for winter 2006 - 2007 saved for comparison with RGPS., https://doi.org/10.5281/zenodo.13302007, 2024a.

430 Korosov, A.: NeXtSIM parameter tuning software, nextsimtuning-0.1, https://doi.org/10.5281/zenodo.13302227, 2024b.

Korosov, A.: Sea ice drift deformation analysis software, pysida-0.1, https://doi.org/10.5281/zenodo.13301869, 2024c.

Korosov, A., Rampal, P., Ying, Y., Ólason, E., and Williams, T.: Towards improving short-term sea ice predictability using deformation observations, The Cryosphere, 17, 4223–4240, https://doi.org/10.5194/tc-17-4223-2023, 2023.

Kwok, R.: Contrasts in sea ice deformation and production in the Arctic seasonal and perennial ice zones, Journal of Geophysical Research, 435 111, https://doi.org/10.1029/2005jc003246, 2006.

Kwok, R., Hunke, E. C., Maslowski, W., Menemenlis, D., and Zhang, J.: Variability of sea ice simulations assessed with RGPS kinematics, Journal of Geophysical Research, 113, https://doi.org/10.1029/2008JC004783, 2008.

Lehoucq, R., Weiss, J., Dubrulle, B., Amon, A., Le Bouil, A., Crassous, J., Amitrano, D., and Graner, F.: Analysis of image vs. position, scale and direction reveals pattern texture anisotropy, Frontiers in Physics, 2, https://doi.org/10.3389/fphy.2014.00084, 2015.

440 Marsan, D. and Weiss, J.: Space/time coupling in brittle deformation at geophysical scales, Earth and Planetary Science Letters, 296, 353–359, https://doi.org/10.1016/j.epsl.2010.05.019, 2010.

Mellor, M.: Mechanical behavior of sea ice, chap. 2, pp. 165–281, NATO ASI Series, Springer US, Boston, MA, https://doi.org/10.1007/978-1-4899-5352-0_3, 1986.

Ólason, E., Boutin, G., Korosov, A., Rampal, P., Williams, T., Kimmritz, M., Dansereau, V., and Samaké, A.: A new brit-
445 tle rheology and numerical framework for large-scale sea-ice models, Journal of Advances in Modeling Earth Systems, 14, https://doi.org/10.1029/2021ms002685, 2022.

Panteleev, G., Yaremchuk, M., Stroh, J. N., Francis, O. P., and Allard, R.: Parameter optimization in sea ice models with elastic–viscoplastic rheology, The Cryosphere, 14, 4427–4451, https://doi.org/10.5194/tc-14-4427-2020, 2020.

Panteleev, G., Yaremchuk, M., and Francis, O.: Reconstruction of the Rheological Parameters in a Sea Ice Model with Viscoplastic Rheology,
450 Journal of Atmospheric and Oceanic Technology, 40, 141 – 157, https://doi.org/10.1175/JTECH-D-21-0158.1, 2023.

Park, J.-W., Korosov, A. A., Babiker, M., Won, J.-S., Hansen, M. W., and Kim, H.-C.: Classification of Sea Ice Types in Sentinel-1 SAR images, The Cryosphere Discussions, 2019, 1–23, https://doi.org/10.5194/tc-2019-127, 2019.

Rampal, P., Bouillon, S., Ólason, E., and Morlighem, M.: neXtSIM: a new Lagrangian sea ice model, The Cryosphere, 10, 1055–1073, https://doi.org/10.5194/tc-10-1055-2016, 2016.

455 Rampal, P., Dansereau, V., Ólason, E., Bouillon, S., Williams, T., Korosov, A., and Samaké, A.: On the multi-fractal scaling properties of sea ice deformation, The Cryosphere, 13, 2457–2474, https://doi.org/10.5194/tc-13-2457-2019, 2019.

Regan, H., Rampal, P., Ólason, E., Boutin, G., and Korosov, A.: Modelling the evolution of Arctic multiyear sea ice over 2000–2018, The Cryosphere, 17, 1873–1893, https://doi.org/10.5194/tc-17-1873-2023, 2023.

Sakov, P., Counillon, F., Bertino, L., Lister, K. A., Oke, P. R., and Korablev, A.: TOPAZ4: An ocean sea ice data assimilation system for the
460 North Atlantic and Arctic, Ocean Science, 8, 633–656, https://doi.org/10.5194/os-8-633-2012, 2012.

Schulson, E. M., Fortt, A. L., Iliescu, D., and Renshaw, C. E.: Failure envelope of first-year Arctic sea ice: The role of friction in compressive fracture, Journal of Geophysical Research, 111, https://doi.org/10.1029/2005JC003235, 2006.

van der Walt, S., Schönberger, J., Nunez-Iglesias, J., Boulogne, F., Warner, J., Yager, N., Gouillart, E., and Yu, T.: scikit-image: image processing in Python, PeerJ, https://doi.org/10.7717/peerj.453, 2014.

465   Vincent, P., Larochelle, H., Bengio, Y., and Manzagol, P.-A.: Extracting and composing robust features with denoising autoencoders, in:
      International Conference on Machine Learning, https://api.semanticscholar.org/CorpusID:207168299, 2008.

Weiss, J. and Schulson, E. M.: Coulombic faulting from the grain scale to the geophysical scale: lessons from ice, Journal of Physics D:
      Applied Physics, 42, 214 017, https://doi.org/10.1088/0022-3727/42/21/214017, 2009.

Williams, T., Korosov, A., Rampal, P., and Ólason, E.: Presentation and evaluation of the Arctic sea ice forecasting system neXtSIM-F, The
470   Cryosphere, 15, 3207–3227, https://doi.org/10.5194/tc-15-3207-2021, 2021.

Zakhvatkina, N., Korosov, A., Muckenhuber, S., Sandven, S., and Babiker, M.: Operational algorithm for ice–water classification on
      dual-polarized RADARSAT-2 images, The Cryosphere, 11, 33–46, https://doi.org/10.5194/tc-11-33-2017, 2017.